Supporting Information

Schushan et al. 10.1073/pnas.0914717107

SI Text

SI Methods ***Further details of model-building and parameterization.***

Sequence data.

We initiated a three-iteration PSI-BLAST (1) search of hCTR1 against the UniProt database (2) with an E-value threshold of 0.0001. Discarding redundant hits (>99% sequence identity) and fragments (<60% of hCTR1's length), we obtained a multiple sequence alignment (MSA) of 271 sequences using MUSCLE (3). We used the MSA to estimate the evolutionary conservation level at each amino acid position via the ConSeq webserver [(4), http://conseq.tau.ac.il].

TM helix boundaries.

In the literature there is overall agreement regarding the core sequence of the three TM helices of hCTR1 (5–9). However, estimates regarding the exact boundaries of each helix differ by up to seven residues. Following an approach that we used previously to model the EmrE transporter (10), we identified the TM helices as the longest hydrophobic stretches in the protein sequence after taking into account the equivalent regions in homologues (11). We extended the hydrophobic stretch detected in the sequence of hCTR1 by including positions in which most of the homologous sequences contained hydrophobic residues. For determining the ends of TM1 and TM3, we also incorporated the evolutionary conservation analysis, which indicated a clear pattern of helix periodicity in both TM segments (Fig. 1*A*). The final helix boundaries were thus set to 69–86 (TM1), 136–154 (TM2) and 160–176 (TM3) (Fig. S1*A*). The boundaries should roughly correspond to the hydrocarbon region of the membrane, and the actual TM helices may extend beyond them.

Selection of helix orientation and construction of noncanonical helices.

Employing the approach of Fleishman et al. (11), we obtained the best-scored helical rotation separately for each of the three helices. Briefly, the algorithm starts from the helix principal axes (extracted from a low-resolution map), and constructs Cα-trace models of the corresponding helices. Next, for predicting the rotational angle of each helix around the axis, the algorithm includes a scoring function that favors the burial of conserved residues in the protein core, as well as the exposure of variable amino-acids to the lipid membrane. In addition, a penalty is associated with orienting any of the amino-acids Asp, Glu, Lys, Arg, and Asn toward the membrane. Calculated individually for each helix, the highest-scored rotation angle is selected using an exhaustive search in which the scores for all orientations are calculated in increments of 5° (Fig. S7).

The original algorithm was only capable of constructing perfectly canonical helices (11). We introduced an improvement in the helix construction section of the algorithm to support also noncanonical helices, which are abundant in TM proteins and are visible in the cryoEM map of hCTR1 (12). Briefly, the principal axes, extracted from the cryoEM map containing the apparent helix kinks, were first divided into a series of points in 3D space. Each point represented the projection of the Cα of a single residue on the principal axis. Every point was set at a distance of 1.5 Å from the previous one to accommodate the known traits of alpha-helices. A virtual disc with a radius of 2.3 Å was built around each point. Each disc was tilted so that its normal was the vector connecting its corresponding point to the next. The disc corresponding to the last point was tilted in the same direction as the previous disc. Next, we placed the Cα atom of each residue on the perimeter of its corresponding disc, rotating each atom by an additional 100° around the disc's perimeter. This maintained the helical periodicity around the principal axes. Because we incorporated the direction vector between each two points to establish the location of the Cα atom, we could model any noncanonical helical structural feature.

Alternative conservation profiles.

CTR proteins are characterized by rather diverse N- and C-termini, varying in both size and residue content. The long loop between TM1 and TM2 also exhibits similar features. Comparing these regions to the three TM regions, it is apparent that the TM parts are indeed much more conserved (Fig. 1*A*). In the ConSeq webserver [(4), http://conseq.tau.ac.il/] the conservation score of each residue is calculated relative to the conservation levels of all positions in a given MSA. Therefore, when we used the full MSA, which included the variable regions in addition to the conserved TM segments, the grades of the TM region had a somewhat limited distribution, with the lowest grade set at five. As expected, removal of the variable regions resulted in a sharper conservation signal in the TM region, with grades ranging from 1 to 9. We therefore constructed a Cα-trace model of hCTR1 using conservation scores based on the full MSA (Fig. 1), the MSA in which the N- and C-termini were extracted, and using an additional MSA in which we also removed the long loop between TM1 and TM2. Reassuringly, all resulting models had almost identical properties; the largest difference was a rotation angle of a single helix in one of the models, which deviated by 5° from those in the other models. This value is much lower than the predicted error range of 20° (see *Discussion* in the main text). Hence, we can estimate that the model structure is robust with respect to changes in the conservation scores, computed based on different MSAs.

TM2-3 loop and model symmetry.

The loop included in the final model structure was constructed using PLOP (13). To estimate the reliability of this loop configuration, we generated 500 additional loop conformations using the kinematic loop closure method, embedded in the recent Rosetta software package (14). The Rosetta-produced loops corresponded to the PLOP conformation, with a large cluster of 308 loops yielding an rmsd of <0.2 Å from the original PLOP loop. Additionally, the manual procedure of extracting the helices' principal axes did not result in an entirely symmetric model. Assuming that the structure is, on average, symmetric, we enforced symmetry on the model using the method of Andre et al. (15), part of the Rosetta package.

Physicochemical characteristics. Although the hCTR1 Cα-trace model provided only a rough estimate of the location of the Cα atoms of the TM domain (see *Discussion* in the main text), it was still sufficient for investigation of the domain's physicochemical properties (Fig. S1*B*). Out of the few hydrophilic residues in TM1 and TM3, Met69, Tyr83, and Glu84 of TM1 along with Cys161 and Tyr172 of TM3 were located at the cytoplasmic edges of their TM segments or were positioned toward neighboring TM helices. The remaining polar residues, Met81 (TM1) and Thr170 (TM3), were exposed to the lipid (Fig. S1*B*), but examination of our alignment of the CTR family revealed that most homologues in fact possess hydrophobic residues in these positions (data available upon request). TM2's hydrophilic residues constitute a single, evolutionarily conserved helical face, composed of the residues His139, Gln142, Ser146, Tyr147, Met150, and Met154 (Fig. 1*B*). The model positioned this conserved polar face toward the pore, creating a hydrophilic environment within the pore (Fig. S1*B*). This orientation corresponded well with the chemical nature of TM2 and its intuitively assigned role in coating the ion translocation pathway. It is noteworthy that these structural features were not direct derivatives of the model-building process, as the scoring function relies mainly on the given conservation profile, with minor penalties for orienting charged amino-acids, as well as Gln, toward the lipids (11).

SI Results *GNM and ANM analysis.*

GNM versus ANM.

In GNM and ANM (16–19), the structure is viewed as a collection of nodes, representing the Cα atoms, and springs, contacting the Cα-atoms within a distance range. The particular topology of the structure determines its collective modes of motion. GNM, being an isotropic and a one-dimensional model, characterizes only the magnitudes of fluctuations; ANM, on the other hand, predicts also the directions of the fluctuations. In GNM, the correlation between the fluctuations $\Delta\mathbf{R}_i$ and $\Delta\mathbf{R}_j$ of residues i and j can be expressed as a sum of individual modes, where N is the number of residues, using:

$$\langle \Delta\mathbf{R}_i \Delta\mathbf{R}_j \rangle = (3k_B T/\gamma)[\Gamma^{-1}]_{ij} = (3k_B T/\gamma)\Sigma_k[\lambda_k^{-1}\mathbf{u}_k\mathbf{u}_k^T]_{ij} \qquad \textbf{[S1]}$$

Here, Γ is the connectivity (or Kirchhoff) matrix, accounting for the interaction of residues within a distance cut-off by a harmonic potential function (with a force constant γ). The term **k** refers to the N-1 nonzero modes; $\lambda_\mathbf{k}$ is the eigenvalue of Γ that refers to the k-th mode of motion; $\mathbf{u}_k$ is the k-th eigenvector; $\mathbf{k_B}$ is the Boltzmann constant; and **T** is the absolute temperature. The contribution of each motion scales with the inverse frequency of that mode. When $i = j$, the predicted correlations are reduced to the mean-square fluctuations of residues. The normalized positive and negative correlations refer, respectively, to fluctuations that are correlated in the same and opposite directions, using:

$$\langle \Delta\mathbf{R}_i \Delta\mathbf{R}_j \rangle_{\text{norm}} = \langle \Delta\mathbf{R}_i \Delta\mathbf{R}_j \rangle / (\langle \Delta\mathbf{R}_i^2 \rangle^{1/2} \langle \Delta\mathbf{R}_j^2 \rangle^{1/2}) \qquad \textbf{[S2]}$$

Of the two elastic models, GNM is more robust in the prediction of fluctuations (18, 20, 21). Thus, it was used here to predict the relative magnitudes of fluctuations of residues, to identify hinge regions and to derive the cooperative motion of the model structure. ANM was then used to predict the directions of motion and to generate the conformations that describe the motion, in accordance with the fluctuations described by the GNM analysis. In this study, we used distance cut-offs of 10 Å and 18 Å for the slowest modes of GNM and ANM, respectively. We performed GNM and ANM analysis using in-house programs, as well as the HingeProt webserver (22). For ANM, we reviewed only non-degenerate motions, as these suggest symmetric motion. We then matched the corresponding GNM and ANM modes according to their square displacements and hinge regions (Table S4). Additionally, high-frequency vibrating residues of the fastest GNM modes were detected using a cut-off of 6.5 Å for the distance between contacting Cα-atoms, as previously established (23–26). Such positions have been shown to correspond to positions essential for fold stabilization or function (25, 26).

Matching GNM and ANM modes.

Although the two elastic network models GNM and ANM differ in their underlying potential functions, studies have demonstrated that, as shown for other systems, modes of motion predicted for TM proteins by GNM and ANM can be related using a comparison between the derived fluctuations [e.g. (27–29)]. While associating GNM and ANM modes, one must keep in mind that minima are more accurately predicted by the GNM model (18, 20, 21). Therefore, we matched the modes taking into account that some of the hinges displayed by the anisotropic ANM model might not be displayed by a matching GNM model (Table S4). Indeed, whereas GNM mode 1,2 displayed a single prominent minimum in the region of M150 and M154, the associated ANM mode 3 included some additional local regions of low mobility (Figs. S3 *A* and *C*). Yet, because the single region identified as a minimum in GNM mode 1,2 is clearly the dominant minimum in ANM mode 3 as well (Movie S1), we concluded that GNM mode 1,2 and ANM mode 3 are matching modes, describing similar motion. We validated our conclusion by mapping of GNM-derived cross-correlations from mode 1,2 on the structural deformations of the third ANM mode. The motion of ANM3 suggested a dynamic domain of three structural units, formed by TM1 and TM3 from the same subunit along with TM2 of an adjacent subunit (Fig. 4 and Movie S1). Indeed, these exact segments were positively correlated according to the matched GNM mode 1,2 (Fig. 3*C*). Clearly, the cross-correlation of GNM3, separating the structure into oppositely correlated cytoplasmic and extracellular parts (Fig. 5*C*), does not match the motion depicted by ANM3 (Fig. 4). The next match, GNM3 and ANM6, was much more intuitive, as the regions of minimal mobility were essentially identical in both modes (Fig. S3 *B* and *D*). In both modes, the hinges were located approximately at the center of the TM helices, resulting in extracellular and intracellular rigid parts. Mapping the cross-correlations of GNM3 on the deformation of ANM6 (Movies S2 and S3), we indeed observed that the dynamics is composed of two distinct cooperative motions: the extracellular parts of the TM helices displayed a rotational movement, whereas the cytoplasmic parts moved toward and back from the pore center. Notably, as GNM mode 3 is very similar to, GNM mode 4,5, whereas ANM mode 6 displays essentially the same motion as ANM mode 7, we extrapolated the match of GNM3 and ANM6 to the similar modes as well (Fig. S3*B*).

Conformation of the TM2-3 Loop.

To examine the robustness of our results, we performed the GNM/ANM analysis using two other models with substantially different loop conformations, obtained using the program Loopy (30). The calculations yielded almost identical results to those obtained with the trimer consisting of the PLOP-generated loop. GNM fluctuation shapes, detected hinge regions, ANM fluctuations and interresidue cooperative dynamics were generally the same for all examined loop conformations, whereas the exact, absolute values of the residue fluctuation magnitudes differed slightly. We thus concluded that the exact loop conformation had negligible effect on the normal mode analysis investigation.

Approximated helix rotation errors: Effect on dynamics and structural interpretation.

As mentioned above, the scoring function we used examined the possible rotation angles in increments of 5°. Plotting the scores for the possible rotational angles, we observed that for each helix there were several sequential rotation angles that received very similar scores (Fig. S7). We thus approximated the expected error in the helix rotations, consisting of three different rotational angles for TM1, four possible orientations for TM2, and four for TM3 (overall $3 \times 4 \times 4 = 48$ alternatives). As both GNM and ANM rely only on Cα-Cα contacts to predict motion, we compared the contacts of all 48 possible models to investigate the effect of this error range on our findings. Reassuringly, the number of differences between the contacts of the selected model and those of the other possible models was small. Of approximately 800 contacts in the TM domain of each model, the number of contact differences ranged from 6 to 24.

To further investigate the matter, we added the TM2-3 loop to the model that had the largest number of altered contacts and carried out the GNM/ANM and structural analysis on that model. Indeed, we received the exact same results for the normalized square displacements and cross-correlations from GNM and for the ANM-based deformations. Mapping the sensitive- and insensitive-to-mutation positions on this alternative model, we concluded that the structural locations of these residues were hardly affected. Considering the rather small error range, we anticipate a similar effect for the other models as well.

Additional GNM slow modes.

In the main text, we focused on the five slowest GNM modes. Overall, we examined how the 30 slowest modes contributed to the protein's motion. The sixth GNM mode and the following mode 7,8 (average of degenerate modes 7 and 8) contributed similarly to the protein's motion, exceeding 1% (Fig. S2). The square displacements of the modes, however, revealed that the hinge regions were quite similar to the previous ones detected in the third mode and in mode 4,5 (Fig. S4*B*) but were more emphasized. We could not match a specific slow ANM mode to these modes and decided not to fully analyze the predicted functional motion associated with these modes. Nevertheless, the most cooperative modes are expected to describe functional motions in biological macromolecules (31).

Highly fluctuating residues: Fastest GNM modes.

The fastest modes of the GNM can be used to identify kinetically hot positions; i.e., positions that are critical for the stabilization of the structure or are involved in binding (23–26). Previous studies have stated that the high-frequency of such residues is a direct consequence of a sheer energy landscape around their highly restricted positions in the structure. These residues undergo fast fluctuations with small conformational freedom. For hCTR1, the eigenvalues of the nine fastest GNM modes revealed three degenerate groups, consisting of modes 1′–3′, 4′–6′ and 7′–9′ (Fig. S6*A*). We identified the most mobile residues in these modes as the most prominent peaks in the fluctuations. Interestingly, these positions consisted of Ala80 of TM1 and GxxxG-contacting residues Gly167 and Gly171 of TM3 (Fig. S6*B*). This suggests a possible role for these residues in structure stabilization or as critical points at the helix-helix interface, as indicated before for high-fluctuating positions. Whereas it was previously speculated that the GxxxG is of structural significance (12, 32), no such role was established for Ala80. It should also be noted that location of the two glycines in the tightest contact point of the structure is not a direct consequence of the modeling approach; the scoring function attempts to maximize the number of buried conserved and exposed variable residues for a single TM helix, without accounting for the size of specific residues included in the segment (11).

1. Altschul SF, et al. (1997) Gapped BLAST and PSI-BLAST: A new generation of protein database search programs. *Nucleic Acids Res* 25(17):3389–3402.
2. Bairoch A, et al. (2005) The universal protein resource (UniProt). *Nucleic Acids Res* 33:D154–D159.
3. Edgar RC (2004) MUSCLE: A multiple sequence alignment method with reduced time and space complexity. *BMC Bioinformatics* 5:113.
4. Berezin C, et al. (2004) ConSeq: The identification of functionally and structurally important residues in protein sequences. *Bioinformatics* 20(8):1322–1324.
5. De Feo CJ, Aller SG, Unger VM (2007) A structural perspective on copper uptake in eukaryotes. *Biometals* 20(3–4):705–716.
6. Sharp PA (2003) Ctr1 and its role in body copper homeostasis. *Int J Biochem Cell B* 35(3):288–291.
7. van den Berghe PV, et al. (2007) Human copper transporter 2 is localized in late endosomes and lysosomes and facilitates cellular copper uptake. *Biochem J* 407(1):49–59.
8. Lee J, Prohaska JR, Dagenais SL, Glover TW, Thiele DJ (2000) Isolation of a murine copper transporter gene, tissue specific expression and functional complementation of a yeast copper transport mutant. *Gene* 254(1–2):87–96.
9. Eisses JF, Kaplan JH (2005) The mechanism of copper uptake mediated by human CTR1: A mutational analysis. *J Biol Chem* 280(44):37159–37168.
10. Fleishman SJ, et al. (2006) Quasi-symmetry in the cryoEM structure of EmrE provides the key to modeling its transmembrane domain. *J Mol Biol* 364(1):54–67.
11. Fleishman SJ, Harrington S, Friesner RA, Honig B, Ben-Tal N (2004) An automatic method for predicting transmembrane protein structures using cryoEM and evolutionary data. *Biophys J* 87(5):3448–3459.
12. De Feo CJ, Aller SG, Siluvai GS, Blackburn NJ, Unger VM (2009) Three-dimensional structure of the human copper transporter hCTR1. *Proc Natl Acad Sci USA* 106(11): 4237–4242.
13. Jacobson MP, et al. (2004) A hierarchical approach to all-atom protein loop prediction. *Proteins* 55(2):351–367.
14. Mandell DJ, Coutsias EA, Kortemme T (2009) Subangstrom accuracy in protein loop reconstruction by robotics-inspired conformational sampling. *Nat Methods* 6(8): 551–552.
15. Andre I, Bradley P, Wang C, Baker D (2007) Prediction of the structure of symmetrical protein assemblies. *Proc Natl Acad Sci USA* 104(45):17656–17661.
16. Atilgan AR, et al. (2001) Anisotropy of fluctuation dynamics of proteins with an elastic network model. *Biophys J* 80(1):505–515.
17. Bahar I, Atilgan AR, Erman B (1997) Direct evaluation of thermal fluctuations in proteins using a single-parameter harmonic potential. *Fold Des* 2(3):173–181.
18. Bahar I, Rader AJ (2005) Coarse-grained normal mode analysis in structural biology. *Curr Opin Struc Biol* 15(5):586–592.
19. Bahar I, Kaplan M, Jernigan RL (1997) Short-range conformational energies, secondary structure propensities, and recognition of correct sequence-structure matches. *Proteins* 29(3):292–308.
20. Cui Q, Bahar I (2006) *Normal Mode Analysis: Theory and Applications to Biological and Chemical Systems* (Chapman & Hall, London).
21. Rader AJ, Chennubhotla C, Yang L-W, Bahar I, Cui Q (2006) The Gaussian network model: Theory and applications. *Normal Mode Analysis—Theory and Applications to Biological and Chemical Systems* (Chapman & Hall, London), pp 41–63.
22. Emekli U, Schneidman-Duhovny D, Wolfson HJ, Nussinov R, Haliloglu T (2008) HingeProt: Automated prediction of hinges in protein structures. *Proteins* 70(4):1219–1227.
23. Demirel MC, Atilgan AR, Jernigan RL, Erman B, Bahar I (1998) Identification of kinetically hot residues in proteins. *Protein Sci* 7(12):2522–2532.
24. Bahar I, Atilgan AR, Demirel MC, Erman B (1998) Vibrational dynamics of folded proteins: Significance of slow and fast motions in relation to function and stability. *Phys Rev Lett* 80(12):2733–2736.
25. Haliloglu T, Erman B (2009) Analysis of correlations between energy and residue fluctuations in native proteins and determination of specific sites for binding. *Phys Rev Lett* 102(8):088103.
26. Haliloglu T, Seyrek E, Erman B (2008) Prediction of binding sites in receptor-ligand complexes with the Gaussian network model. *Phys Rev Lett* 100(22):228102.
27. Shrivastava IH, Bahar I (2006) Common mechanism of pore opening shared by five different potassium channels. *Biophys J* 90(11):3929–3940.
28. Haliloglu T, Ben-Tal N (2008) Cooperative transition between open and closed conformations in potassium channels. *PLoS Comput Biol* 4(8):e1000164.
29. Isin B, Rader AJ, Dhiman HK, Klein-Seetharaman J, Bahar I (2006) Predisposition of the dark state of rhodopsin to functional changes in structure. *Proteins* 65(4):970–983.
30. Xiang Z, Soto CS, Honig B (2002) Evaluating conformational free energies: The colony energy and its application to the problem of loop prediction. *Proc Natl Acad Sci USA* 99(11):7432–7437.
31. Bahar I, Lezon TR, Bakan A, Shrivastava IH (2009) Normal mode analysis of bBiomolecular structures: Functional mechanisms of membrane proteins. *Chem Rev* 110(3):1463–1497.
32. Aller SG, Eng ET, De Feo CJ, Unger VM (2004) Eukaryotic CTR copper uptake transporters require two faces of the third transmembrane domain for helix packing, oligomerization, and function. *J Biol Chem* 279(51):53435–53441.

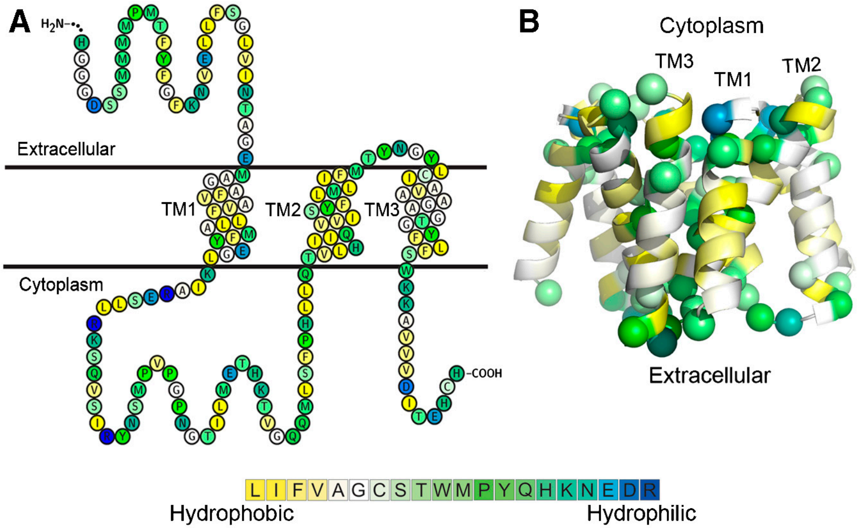

Fig. S1. Physicochemical properties of the hCTR1 model structure. (*A*) The hCTR1 sequence is colored according to hydrophobicity (1), using the blue-to-yellow color code shown in the color bar. The predicted boundaries of the three TM segments are marked. For clarity, only part of the N-terminal is illustrated. (*B*) Side view of the hCTR1 model colored similarly according to hydrophobicity (1), with Cα-atoms of hydrophilic residues shown as spheres and the cytoplasmic side facing up. It is apparent that the pore is enriched with hydrophilic residues, whereas the membrane-facing positions are mostly hydrophobic, as expected.

[1] Kessel A, Ben-Tal N (2002) *Peptide–Lipid Interactions: Current Topics in Membranes* ed Simon S (Academic, San Diego) Vol 52, pp 205–253.

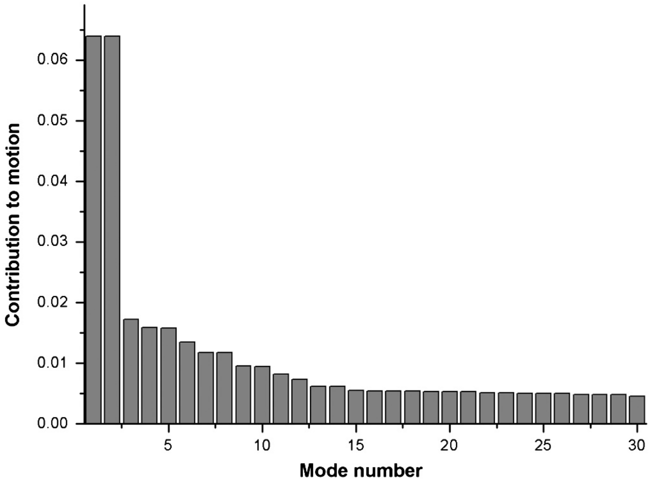

Fig. S2. Contribution of slow GNM modes to motion. The contribution of the 30 slowest GNM modes to the overall motion, based on their eigenvalues. This graph reveals pairs of degenerate modes, displaying the same eigenvalues, e.g. modes 1 and 2, 4 and 5, 7 and 8, etc.

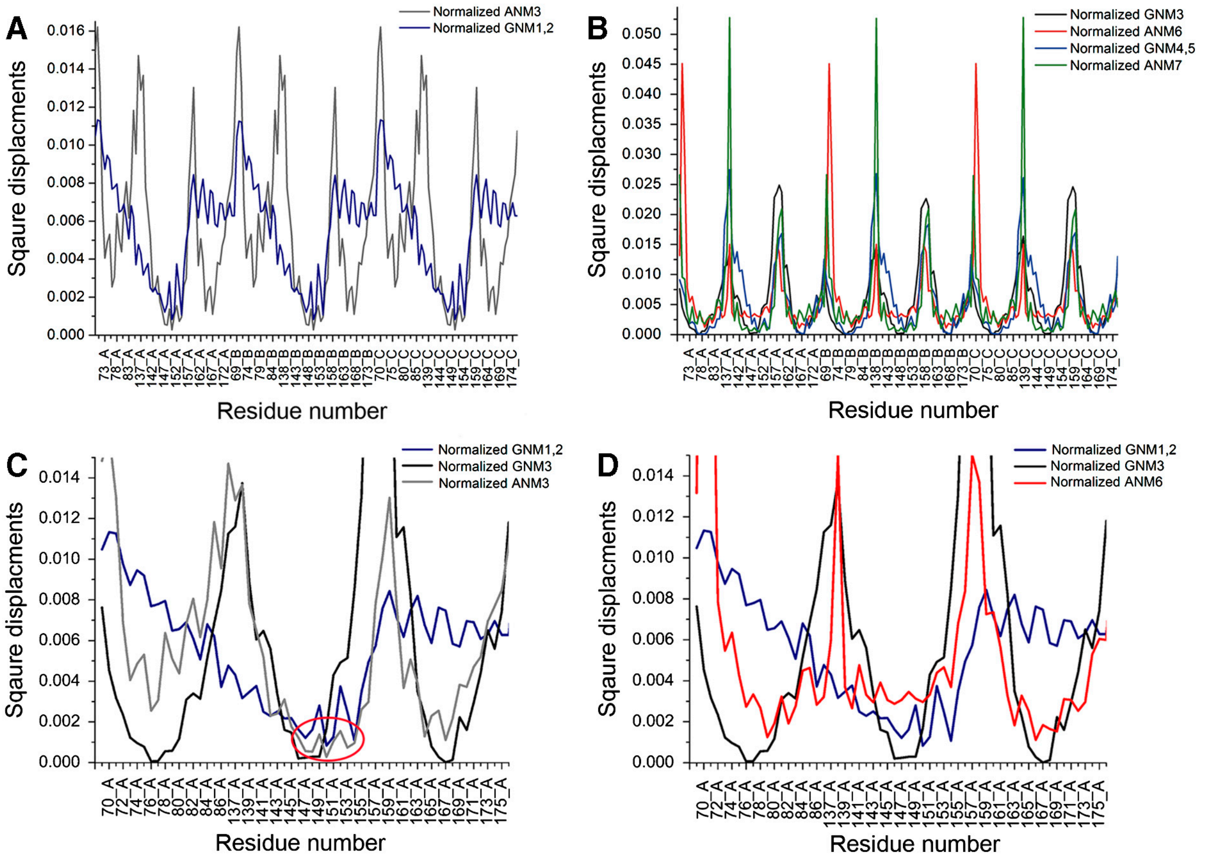

Fig. S3. Associated slowest GNM and ANM modes. The square fluctuations of GNM and ANM modes are displayed according to the legend. The residue numbers are shown with their corresponding chains. For clarity, in panels C and D fluctuations of only one chain is displayed, and the maximum value is set to 0.014. (*A*) GNM1,2 is matched to ANM3, with the most prominent minima emerging in Met150 and Met154 of the TM2 MxxxM motif in both modes. (*B*) GNM3, GNM4,5 and ANM modes 6 and 7 display essentially the same square displacements, with minima as marked in Fig. 5*A*, including residues of the GxxxG motif. (*C*) GNM1,2 and GNM3 compared to ANM3. Although ANM3 does display some local minima around positions 77 and 168, the most prominent hinge (encircled) is located at positions 147, 150 and 154, matching exactly the dominant minima of GNM1,2. (*D*) GNM1,2 and GNM3 compared to ANM6. ANM6 displays three equally emphasized minima regions, corresponding to the minima of GNM3. GNM1,2, on the other hand, consists of a single hinge region, therefore probably does not match this ANM mode.

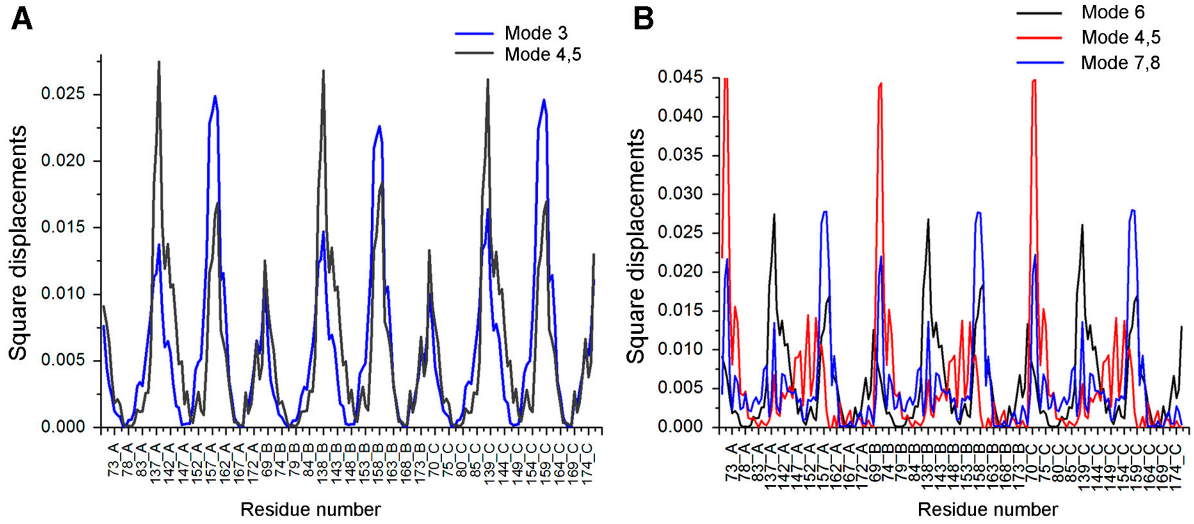

Fig. S4. Comparison of slow GNM modes. Square displacements are shown for the three subunits according to the legend. The residue numbers are shown with their corresponding chains. (*A*) Mode 3 and mode 4,5 (average of modes 4 and 5). The modes exhibit similar hinge regions, located approximately at residues 75–80, 145–150 and 165–170 of TM1, TM2 and TM3, respectively. (*B*) Modes 6 and 7,8 to mode 4,5. Slow modes 6 and 7,8 exhibit similar hinge regions to mode 4,5, albeit some hinge regions are more emphasized or expanded beyond their regions in mode 4,5.

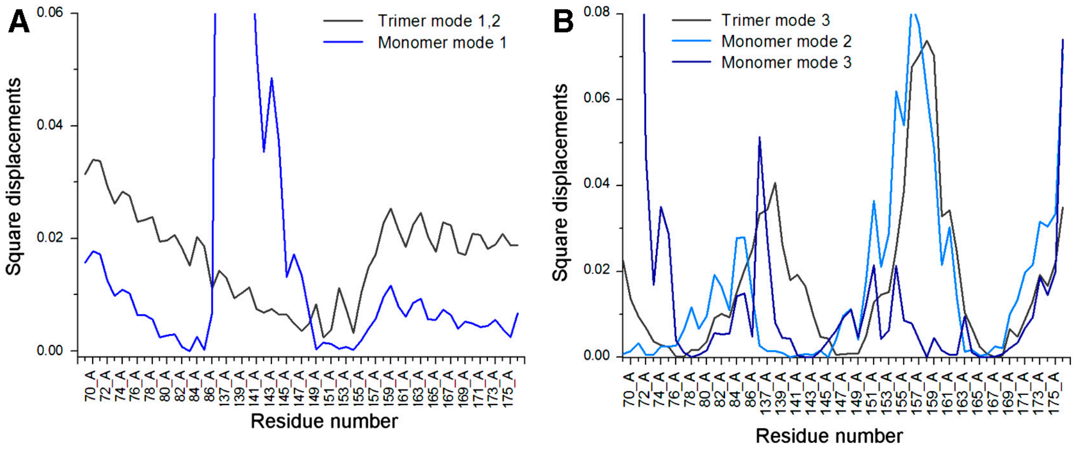

Fig. S5. The GNM analysis of the hCTR1 monomer shows, in essence, the same results obtained for the trimer. We carried out GNM calculations for the hCTR1 monomer as described above for the trimer. In both panels, the fluctuations of the slowest GNM modes obtained for the isolated monomer are compared to those of the trimeric structure. The residue numbers are shown with their corresponding chains. (*A*) GNM mode 1,2 of the trimer was compared to the slowest mode of motion of the monomer. It is apparent that minima appear in similar regions, with the slowest mode of the monomer showing an additional hinge compared to GNM mode 1,2 of the trimer. (*B*) The shape of the third trimeric GNM mode is similar to those of the second and third slowest monomeric modes.

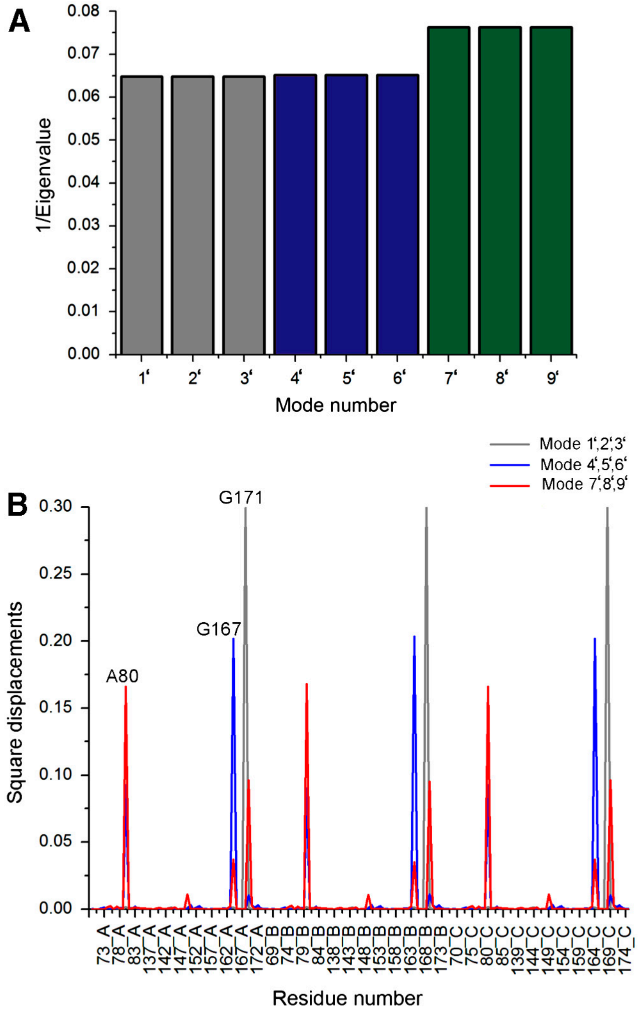

Fig. S6. The fastest GNM modes. (*A*) Contribution to motion of the nine fastest GNM modes. It is evident that there are three groups of degenerate modes, modes 1′–3′, 4′–6′ and 7′–9′, with 1/eigenvalues of 0.064778, 0.065116 and 0.076283, respectively. Indeed, superimposing the square displacements resulted in symmetrically shaped graphs for all three groups [in (*B*)]. (*B*) Square displacements of the fastest GNM modes, shown according to the legend above. The detected "kinetically hot" residues are marked on one of the subunits.

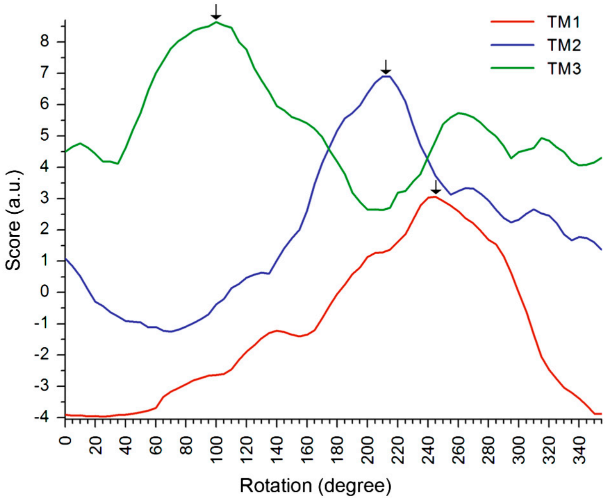

Fig. S7. Score versus rotation angle for each of the three TM helices. A single peak was obtained for each helix, representing its preferable rotation angle. The peaks are marked by the arrows. The final model was generated using the rotation angles with the highest scores.

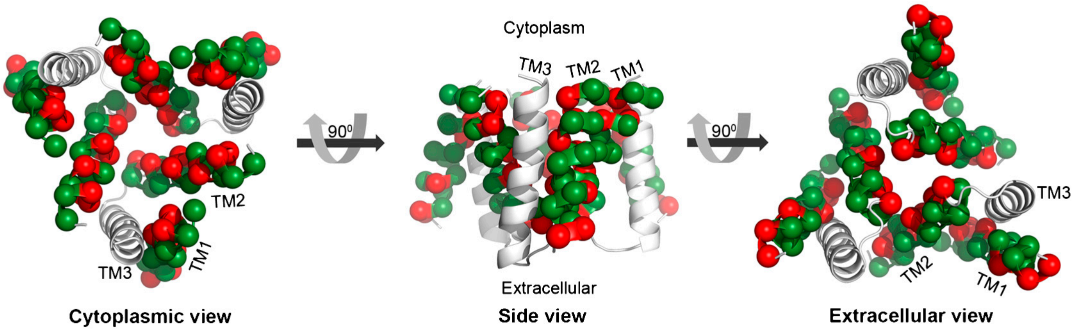

Fig. S8. Emerging experimental data supports the hCTR1 model structure. The hCTR1 model is presented and colored as in Fig. 2 but the positions are now colored according to the new Trp scanning presented in a recently published paper (1). It is evident that the new experimental data agrees with the model structure as well; as determined in previous mutagenesis studies, predicted pore-lining residues are sensitive to mutations. In positions that are lipid-exposed, substitution to Trp is generally tolerated. Notably, Glu84 and His139, suggested by our study to be engaged in pH dependency, are both sensitive to mutation to Trp.

1 De Feo CJ, Mootien S, Unger VM (2010) Tryptophan scanning analysis of the membrane domain of CTR-copper transporters. *J Membrane Biol* 234(2):113–123.

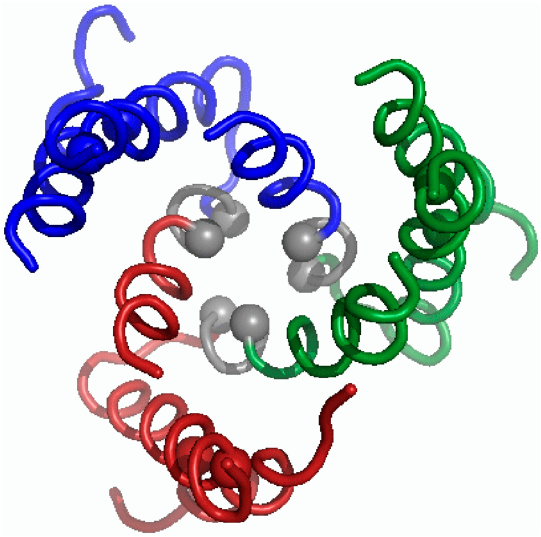

Movie S1. The third ANM mode, corresponding to GNM mode 1,2 (Table S4). The model structure is shown as ribbon and viewed from the cytoplasm. The mode depicts three separate structural elements (red, green, and blue), in accordance with the cooperative dynamics in GNM mode 1,2 (Fig. 3*C*). Each element is composed of TM1 and TM3 of the same chain, along with the N-terminal part of TM2 from an adjacent chain. Gly167 and Gly171 of the GxxxG TM3 motif of the three subunits are depicted as red, green, and blue spheres. The hinge region at the end of TM2, remaining static during motion, is colored gray, with Met150 and Met154 represented by spheres. Residues 85, 86, and 136–139 of the ends of TM1 and TM2, respectively, were omitted for clarity.

Movie S1 (GIF)

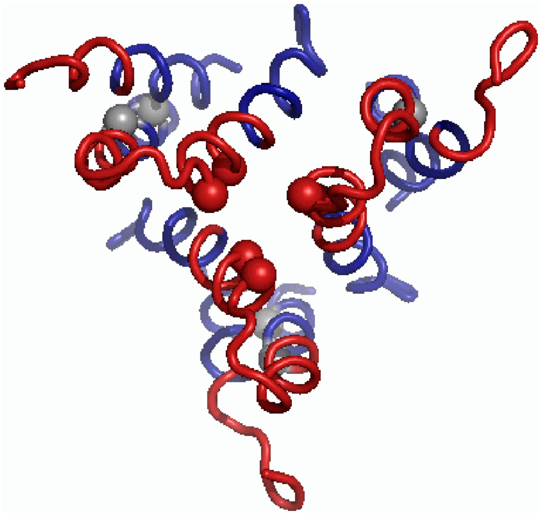

Movie S2. The sixth ANM mode [matched to GNM mode 3 (Table S4)]: An extracellular view. The trimer is colored according to the positive and negative correlations exhibited in the corresponding (third) GNM mode, as in Fig. 5*C*. Spheres represent Met150 and Met154 of the MxxxM TM2 motif and Gly167 and Gly171 of the GxxxG TM3 motif. The glycines, situated at or near the hinge points, are colored gray. The extra- and intracellular helical segments display correlated motion, respectively. Thr136 was omitted for clarity.

Movie S2 (GIF)

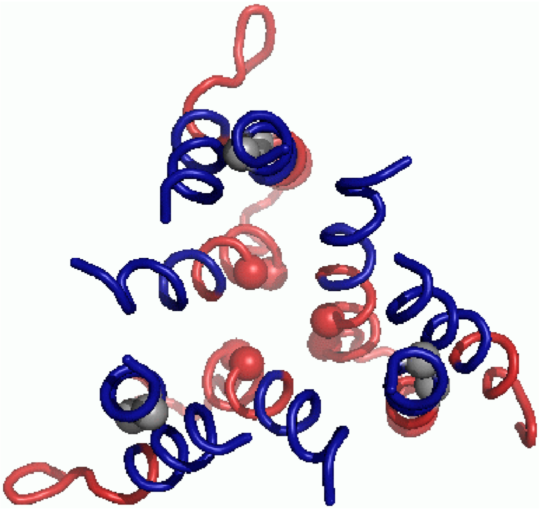

Movie S3. The sixth ANM mode: A cytoplasmic view. The model structure is depicted and colored as in Movie S2, but viewed from the opposite end. Positions 136–137 were omitted for clarity.

Movie S3 (GIF)

Table S1. Scores computed for all 12 possible models

(A,B,C)*	N-terminus outside	N-terminus inside
(1,2,3)	54.29[†]	44.44
(1,3,2)	44.36	38.07
(3,1,2)	33.90	34.96
(3,2,1)	40.09	39.38
(2,1,3)	43.34	45.87
(2,3,1)	38.52	44.90

*Columns A, B, and C correspond to map density rods according to the selected helix assignment, with A, B, and C, matching TM1, TM2, and TM3, representing the selected assignment. The numbers represent altered assignments; for example (1,3,2) represents an assignment in which the TM2 is switched with TM3 relative to the preferred assignment (1,2,3). For each assignment, the scores computed for the correct topology (N-terminus outside the cell) and the inverted one (N-terminus inside the cell) are shown in the two rightmost columns.

[†] The model with the helix assignment and topology suggested in a previous study (12) received a significantly higher score than did all other possible permutations.

Table S2. Available mutagenesis data within the TM region

Substitution (hCTR1 equivalent*)	Pos.	Examined protein	Effect[†]	Con. (1–9)[‡]	Ref.
M69I	TM1	hCTR1	Nondeleterious	8	(1)
M81I	TM1	hCTR1	Nondeleterious	7	(1)
C48S (F73)	TM1	yCTR3	Partial	8	(2)
C51S (V76)	TM1	yCTR3	Partial	8	(2)
Y83A	TM1	hCTR1	Nondeleterious	7	(1)
Y83F	TM1	hCTR1	Deleterious	7	(1)
E84L	TM1	hCTR1	Nondeleterious	9	(1)
E84Q	TM1	hCTR1	Nondeleterious	9	(1)
H139A	TM2	hCTR1	Deleterious	8	(1)
H139R	TM2	hCTR1	Nondeleterious	8	(1)
Y147A	TM2	hCTR1	Nondeleterious	9	(1)
Y147F	TM2	hCTR1	Deleterious	9	(1)
M150L	TM2	hCTR1	Deleterious	9	(3)
M150Q	TM2	hCTR1	Deleterious	9	(4)
M154L	TM2	hCTR1	Deleterious	9	(3)
M154Q	TM2	hCTR1	Deleterious	9	(4)
M150IM154I	TM2	hCTR1	Deleterious	9,9	(1)
Y156A	TM2-3	hCTR1	Deleterious	8	(1)
C161S	TM3	hCTR1	Nondeleterious	8	(1)
I196W (C161)	TM3	yCTR3	Partial	8	(5)
I197W (I162)	TM3	yCTR3	Partial	7	(5)
S198W (A163)	TM3	yCTR3	Deleterious	9	(5)
C199W (V164)	TM3	yCTR3	Deleterious	9	(5)
C199S (V164)	TM3	yCTR3	Nondeleterious	9	(2)
L200W (A165)	TM3	yCTR3	Nondeleterious	8	(5)
I201W (A166)	TM3	yCTR3	Nondeleterious	6	(5)
G167L	TM3	hCTR1	Deleterious	9	(5)
G167S	TM3	hCTR1	Deleterious	9	(4)
G202L (G167)	TM3	yCTR3	Deleterious	9	(5)
G202W (G167)	TM3	yCTR3	Deleterious	9	(5)
A203W (A168)	TM3	yCTR3	Nondeleterious	8	(5)
I204W (G169)	TM3	yCTR3	Nondeleterious	7	(5)
V205W (T170)	TM3	yCTR3	Nondeleterious	6	(5)
G171L	TM3	hCTR1	Deleterious	9	(5)
G206L (G171)	TM3	yCTR3	Deleterious	9	(5)
G206W (G171)	TM3	yCTR3	Deleterious	9	(5)
R207W (Y172)	TM3	yCTR3	Partial	8	(5)
F208W (F173)	TM3	yCTR3	Nondeleterious	7	(5)

*Performed mutation, and corresponding hCTR1 position in cases which the substitution was performed on a homologous protein.

[†] Substitutions were deemed deleterious in cases which this was the observed phenotype, or when mutations reduced activity below 50% of the WT Vmax. Nondeleterious effect was ascribed to substitutions in which this was the determined phenotype, or when activity of over 50% WT Vmax was observed for the mutant. Partial activity was attributed to mutants when this was the observed effect.

[‡] Evolutionary conservation grades for each position, as shown in Fig. 1.

1 Eisses JF, Kaplan JH (2005) The mechanism of copper uptake mediated by human CTR1: A mutational analysis. *J Biol Chem* 280(44):37159–37168.
2 Pena MM, Puig S, Thiele DJ (2000) Characterization of the *Saccharomyces cerevisiae* high affinity copper transporter Ctr3. *J Biol Chem* 275(43):33244–33251.
3 Puig S, Lee J, Lau M, Thiele DJ (2002) Biochemical and genetic analyses of yeast and human high affinity copper transporters suggest a conserved mechanism for copper uptake. *J Biol Chem* 277(29):26021–26030.
4 Liang ZD, Stockton D, Savaraj N, Tien Kuo M (2009) Mechanistic comparison of human high-affinity copper transporter 1-mediated transport between copper ion and cisplatin. *Mol Pharmacol* 76(4):843–853.
5 Aller SG, Eng ET, De Feo CJ, Unger VM (2004) Eukaryotic CTR copper uptake transporters require two faces of the third transmembrane domain for helix packing, oligomerization, and function. *J Biol Chem* 279(51):53435–53441.

Table S3. Distribution of mutated positions on the different locations on the model structure

Class/location	Lipid-exposed	Helix–helix interface	Pore
Deleterious	0	6	4
Nondeleterious	7	2	0
Partial	1	4	0

The mutated positions (Table S2) were divided according to the effect of the substitution on function and the positions' predicted structural locations according to the hCTR1 TM model.

Table S4. Matching GNM and ANM modes

Mode\hinge region	75–80	145–148	147–154	165–170
GNM mode 1,2	–	–	+	–
Third ANM	–	+	+	–
Third GNM	+	+	–	+
GNM mode 4,5	+	+	+	+
Sixth ANM	+	+	+	+
Seventh ANM	+	+	+	+

Each column represents a detected hinge region in the slowest GNM/ANM modes. Corresponding modes are shaded with the same color, matched by analogy between their hinge regions.